AIAA JOURNAL
Vol. 46, No. 10, October 2008

Implicit Large-Eddy Simulation of a Deep Cavity Using High-Resolution Methods

B. Thornber* and D. Drikakis†
Cranfield University, Cranfield, England MK43 0EB, United Kingdom

DOI: 10.2514/1.36856

Implicit large-eddy simulations of a deep cavity at Mach 0.8 and a Reynolds number based on a cavity length of 860,000 were conducted using a modified high-resolution implicit large-eddy-simulation method. The object of the paper is to assess the capability of the modified numerical method compared to large-eddy simulation with a selective mixed-scale model and experimental measurements of the mean flowfield, Reynolds stresses, and pressure spectra. The frequency and amplitude of the fundamental modes are predicted to within 2% and 6 dB at all grid levels. There is excellent agreement of the mean flowfield and Reynolds stresses, demonstrating that there is no need for an explicit subgrid model when using the new reconstruction method for this flow configuration.

Nomenclature

a	=	speed of sound, m/s
D	=	cavity depth, m
e	=	total energy, kg/ms^2
f	=	frequency, Hz
L	=	cavity length, m
M	=	Mach number
$\mathbf{P}$	=	vector of primitive variables
p	=	pressure, N/m^2
Re	=	Reynolds number
U	=	freestream velocity, m/s
u, v, w	=	Cartesian velocity components, m/s
u', v', w'	=	Cartesian fluctuating velocity components, m/s
x, y, z	=	Cartesian coordinates, m
α	=	acceleration, m/s^2
Δx	=	mesh spacing, m
ϵ	=	kinetic energy decay rate, m^2/s^3
μ	=	dynamic viscosity, kg/ms
ν	=	kinematic viscosity, m^2/s
ρ	=	density kg/m^3
ϕ	=	limiter function

I. Introduction

SINCE the early experiments of Rossiter [1], the behavior of high Reynolds number turbulent flow over a cavity has been studied extensively. Cavity flows exhibit a complex feedback mechanism. Small perturbations in the flow upstream of the cavity pass over the leading edge and become unstable, generating Kelvin–Helmholtz vortices. When these structures impact on the trailing edge of the cavity, strong acoustic waves are generated. These acoustic waves then interact and perturb the oncoming shear layer, generating resonance at certain harmonic frequencies.

The most familiar product of this self-sustained oscillation can be heard when driving at modest speed with an open sunroof. If the manufacturer has not added a device to deflect the shear layer over the open cavity, the turbulent layer impacts on the back of the sunroof, causing loud wind buffeting. At high Mach numbers, this becomes a severe issue, leading to vibration and structural fatigue in aircraft wheel bays [2] or weapons bays. Strong oscillations can be a significant issue in the design of store separation mechanisms, due to buffeting of the ordnance [3]. The sharp density gradients generated can refract light rays passing into the cavity, causing distortion when using optical instruments. Cavity flows are also relevant in the design of flameholding geometries for scramjet engines, providing a stable flowfield to prevent flame extinction [4]. It is essential to develop and validate numerical methods that are capable of correctly resolving the flow physics to aid in the design of cavities that mitigate such problematic feedback mechanisms.

Detailed experimental results for a deep open cavity with an aspect ratio L/D of 0.42 at Mach 0.8 and Reynolds 860,000 have been measured by Forestier et al. [5]. A schematic of the experimental setup is shown in Fig. 1. The flow enters the test section with a freestream velocity U of 258 m/s, equivalent to Mach 0.8. The stagnation pressure and temperature were 0.98×10^5 Pa and 293 K, respectively. The cavity length L is 0.05 m, depth is 0.12 m, and width is 0.12 m. The Reynolds number based on cavity length is $Re_c = UL/\nu = 860,000$. Boundary-layer transition was triggered well before the cavity and the incompressible shape factor and momentum thickness were measured as approximately 1.3 and 0.65 mm, respectively.

The experiment measured velocity components using a two-dimensional laser Doppler velocimeter, which were then postprocessed to separate mean flow and Reynolds stresses. In addition, pressure data were taken from a sensor mounted 0.035 m below the lip of the cavity on the upstream face. This measured a strong fundamental mode at a frequency of 1990 ± 6 Hz of magnitude 155 dB and several subsequent harmonics. A semi-empirical formula proposed by Rossiter [1] is commonly used to estimate the frequency of the fundamental mode:

$$f_n = \frac{U}{L}\frac{n-\alpha}{M+1/\kappa} \tag{1}$$

where n is the mode, M is the Mach number, U is the freestream velocity, and κ and α are parameters that are recommended to be 0.57 and 0.25, respectively, for this geometry [1]. However, using the standard coefficients for this geometry gives a predicted fundamental mode at 1515 Hz, an error of almost 30%. This highlights the case for numerical simulation, because for this geometry, the standard empirical formulas are inaccurate. Following their experimental results, Forestier et al. [5] suggest using $\alpha = 0$ for this specific geometry, giving the fundamental mode at 2020 Hz.

Presented as Paper 0730 at the 46th AIAA Aerospace Sciences Meeting and Exhibit, Reno, NV, 7–10 January 2008; received 27 January 2008; revision received 15 May 2008; accepted for publication 19 May 2008.

*Research Fellow, Fluid Mechanics and Computational Science Group, Department of Aerospace Sciences, School of Engineering. Member AIAA.
†Professor, Head, Fluid Mechanics and Computational Science Group, Department of Aerospace Sciences, School of Engineering. Senior Member AIAA.

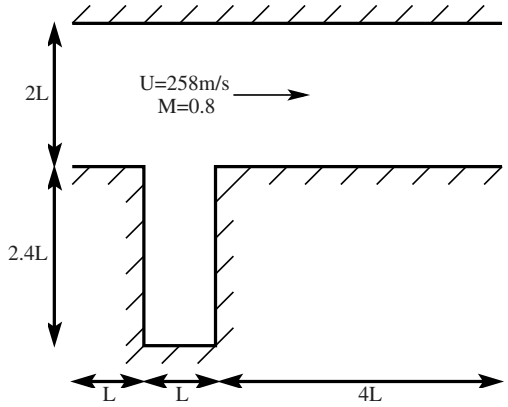

Fig. 1 Schematic of the cavity-flow experimental setup. The width of the channel is 2.4*L*.

Because the cavity flow is at a high Reynolds number, it is not computationally viable to employ direct numerical simulation. Reynolds-averaged Navier–Stokes methods can successfully predict the location of the first mode, but not the magnitude [6]. This is due to the excess dissipation of the Reynolds-averaged Navier–Stokes method in the developing mixing layer, which is inherently unsteady on a short timescale. Large-eddy simulation (LES) is a viable alternative in flows of industrial interest in which the time-dependent behavior of the flow must be resolved. This reduces the required degrees of freedom of the physical system by modeling the influence of the small scales on the large scales. As the acoustic field is simulated directly, this method is commonly denoted as computational aeroacoustics, in which the full Navier–Stokes equations are solved to gain the acoustic field. Previous LES by Larcheveque et al. [6] of this flow configuration gained excellent results using both LES with a selective mixed-scale model and implicit LES (LES with no explicit subgrid model). However, the underlying compressible schemes employed were not shock-capturing, and hence would generate oscillatory behavior at discontinuities.

Recent analysis of the dissipation of kinetic energy within the Godunov scheme [7] have led to the development of a variable reconstruction method that significantly improves on the low Mach performance of standard Godunov schemes, without significantly influencing the shock-capturing ability, positivity preserving, or stability of the underlying numerical method [8]. This improvement in the resolution of low Mach flow features gives a significant improvement in accuracy at high wave numbers in turbulent flows [8]. It is fifth-order-accurate in space (away from maxima and minima), coupled with a third-order-accurate Runge–Kutta time-marching method.

Because no explicit subgrid model is employed, this method falls into the class of implicit LES (ILES) methods. It was first observed by Boris et al. [9] and Youngs [10] that simulating the unfiltered flow equations instead of the filtered equations gives good results in both decaying homogeneous turbulence and mixing flows. Fureby et al. [11] compared and contrasted eight modeling strategies (including no model) using grid sizes of 16^3, 32^3, and 64^3 in the simulation of homogeneous decaying turbulence. The turbulent kinetic energy spectra were compared with the direct numerical simulation of Jimenez et al. [12] and demonstrated that there were only small differences in the macroscopic behavior of the flow for simulations with and without a subgrid model. The basis of this methodology is the observation that the inherent dissipation of the numerical method can remove grid-scale kinetic energy in a manner similar to a conventional subgrid model employed as part of a stable numerical method [13,14]. Numerical approaches employed for ILES are varied and were applied to flows such as Rayleigh–Taylor and Richtmyer–Meshkov instabilities [10,15,16], free jets [9,17], channel flows [17], open cavity flows [6,18,19], geophysical flows [20,21], delta wings [22], and decaying turbulence [11,23–28].

The layout of this paper is as follows. Section II details the governing equations solved and the numerical methodology. The new method is compared briefly with the van Leer and weighted essentially nonoscillatory (WENO) ninth-order methods in simulations of homogeneous decaying turbulence. Comparisons with experimental data for simulated mean flow, Reynolds stresses, and sound pressure levels for the deep-cavity flow are presented in Sec. III. These show excellent agreement with experimental data and conventional LES [6] for all flow quantities. This clearly demonstrates that the new reconstruction method in the ILES framework performs as well as conventional LES without sacrificing shock-capturing capability.

II. Numerical Framework

A. Governing Equations

The physics of (Newtonian) fluid flow are governed by the Navier–Stokes equations. They are solved by considering the coupled generalized conservation laws: namely, the continuity, momentum, and energy equations:

$$\frac{\partial \rho}{\partial t} + \nabla \cdot (\rho \mathbf{u}) = 0 \tag{2}$$

$$\frac{\partial \rho \mathbf{u}}{\partial t} + \nabla \cdot (\rho \mathbf{u}\mathbf{u}) = -\nabla \cdot \mathbf{P} \tag{3}$$

$$\frac{\partial e}{\partial t} + \nabla \cdot (e\mathbf{u}) = -\nabla \cdot (\mathbf{P} \cdot \mathbf{u}) - \nabla \cdot \mathbf{q} \tag{4}$$

where $\mathbf{u}$, ρ, e, and $\mathbf{q}$ stand for the velocity components, density, total energy per unit volume, and heat flux, respectively. The tensor $\mathbf{P}$ for a Newtonian fluid is defined by

$$\mathbf{P} = p(\rho, T)\mathbf{I} + \tfrac{2}{3}\mu(\nabla \cdot \mathbf{u})\mathbf{I} - \mu[(\nabla \mathbf{u}) + (\nabla \mathbf{u})^T] \tag{5}$$

where $p(\rho, T)$ is the scalar pressure, $\mathbf{I}$ is the identity tensor, T is the temperature, and μ is the dynamic viscosity coefficient. The preceding system is completed by an equation of state. For a perfect gas, the equation of state is given by $p = \rho RT$, where R is the gas constant.

To facilitate the development of numerical methods, Eqs. (2–4) are written in Cartesian matrix form as [13]

$$\frac{\partial \mathbf{U}}{\partial t} + \frac{\partial \mathbf{E}}{\partial x} + \frac{\partial \mathbf{F}}{\partial y} + \frac{\partial \mathbf{G}}{\partial z} = \frac{\partial \mathbf{R}}{\partial x} + \frac{\partial \mathbf{S}}{\partial y} + \frac{\partial \mathbf{L}}{\partial z} \tag{6}$$

where $\mathbf{U}$ is the array of the conservative variables; $\mathbf{E}$, $\mathbf{F}$, and $\mathbf{G}$ are the inviscid and $\mathbf{R}$, $\mathbf{S}$, and $\mathbf{L}$ are the viscous flux vectors associated with the Cartesian x, y, and z directions, respectively:

$$\mathbf{U} = [\rho, \rho u, \rho v, \rho w, e]^T,$$

$$\mathbf{E} = [\rho u, \rho u^2 + p, \rho uv, \rho uw, (e + p)u]^T,$$

$$\mathbf{F} = [\rho v, \rho uv, \rho v^2 + p, \rho vw, (e + p)v]^T,$$

$$\mathbf{G} = [\rho w, \rho uw, \rho vw, \rho w^2 + p, (e + p)w]^T,$$

$$\mathbf{R} = [0, \tau_{xx}, \tau_{xy}, \tau_{xz}, u\tau_{xx} + v\tau_{xy} + w\tau_{xz} - \dot{q}_x]^T,$$

$$\mathbf{S} = [0, \tau_{yx}, \tau_{yy}, \tau_{yz}, u\tau_{yx} + v\tau_{yy} + w\tau_{yz} - \dot{q}_y]^T,$$

$$\mathbf{L} = [0, \tau_{zx}, \tau_{zy}, \tau_{zz}, u\tau_{zx} + v\tau_{zy} + w\tau_{zz} - \dot{q}_z]^T$$

The inviscid part of the Navier–Stokes equations are solved using the direction-split approach (also termed the *method of lines*). This involves solving the following governing equations in each principal direction:

$$\frac{\partial \mathbf{U}}{\partial t} + \frac{\partial \mathbf{E}}{\partial x} = 0 \tag{7}$$

Subsequently, the viscous terms are solved via a central-difference scheme.

B. Computational Method

The direction-split method involves two main stages. For first-order accuracy, the fluxes are computed from the solution to the Riemann problem at the cell interface using the left and right quantities. The simulations detailed in this paper employ the HLLC (Harten–Lax–van Leer contact) approximate Riemann solver [29]. Higher-order accuracy is achieved using MUSCL extrapolation [30]:

$$\mathbf{P}^{L}_{i+1/2} = \mathbf{P}_i + \tfrac{1}{2}\phi^{\lim}(r_i^{\lim,L})(\mathbf{P}_i - \mathbf{P}_{i-1}) \tag{8}$$

$$\mathbf{P}^{R}_{i+1/2} = \mathbf{P}_{i+1} - \tfrac{1}{2}\phi^{\lim}(r_i^{\lim,R})(\mathbf{P}_{i+2} - \mathbf{P}_{i+1}) \tag{9}$$

where $\mathbf{P}$ is the vector of cell-averaged primitive variables, and the cells are labeled by the integer i. Also,

$$r_i^{\lim,L} = \frac{\mathbf{P}_{i+1} - \mathbf{P}_i}{\mathbf{P}_i - \mathbf{P}_{i-1}}, \qquad r_i^{\lim,R} = \frac{\mathbf{P}_i - \mathbf{P}_{i-1}}{\mathbf{P}_{i+1} - \mathbf{P}_i} \tag{10}$$

The fifth-order limiter proposed by Kim and Kim [31] is employed:

$$\phi *^{\lim}_{M5,L} = \frac{-2/r_{i-1}^{\lim,L} + 11 + 24r_i^{\lim,L} - 3r_i^{\lim,L}r_{i+1}^{\lim,L}}{30} \tag{11}$$

$$\phi *^{\lim}_{M5,R} = \frac{-2/r_{i+2}^{\lim,R} + 11 + 24r_{i+1}^{\lim,R} - 3r_{i+1}^{\lim,R}r_i^{\lim,R}}{30} \tag{12}$$

where monotonicity is maintained by limiting the preceding extrapolations using

$$\phi^{\lim}_{M5,L} = \max(0, \min(2, 2r_i^{\lim,L}, \phi*^{\lim}_{M5,L})) \tag{13}$$

$$\phi^{\lim}_{M5,R} = \max(0, \min(2, 2r_i^{\lim,R}, \phi*^{\lim}_{M5,R})) \tag{14}$$

This limiter was modified to significantly improve performance in resolving fine-scale motion, particularly at low Mach. Theoretical analysis of the Godunov method has shown that the leading-order dissipation of kinetic energy ϵ can be expressed as [8]

$$\epsilon^{M5} = \frac{\Delta x^5}{60} a u_x u_{xxxxx} + \text{ higher-order terms} \tag{15}$$

where u is the velocity normal to the cell interface, a is the local speed of sound, and Δx is the length of the computational cell. Local means that the quantities are some average of the extrapolated variables or the cell-averaged quantities to either side of the interface. The key observation regarding this result is that the dissipation is proportional to the speed of sound at leading order. This is the source of excessive low Mach dissipation of kinetic energy when employing Godunov methods, such as the results obtained by Volpe [32]. For this reason, the standard MUSCL extrapolation was augmented using the method of Thornber et al. [8], which ensures uniform dissipation of kinetic energy in the limit of zero Mach number. This modification extends the validity of the Godunov method to at least $M \approx 10^{-4}$, via a progressive central differencing of the velocity components, without changing the formulation of the underlying governing equations or sacrificing monotonicity of the density field. It was shown that the leading-order kinetic energy dissipation rate is proportional to $u^3/\Delta x$, similar in form to that proposed by Kolmogorov [33] for decaying turbulence [8]. It is this dissipation rate that acts as a subgrid model in the ILES framework, giving significantly improved high-wave-number performance compared with standard Godunov methods.

This method was compared with the van Leer limiter [30] and ninth-order WENO [34] for the canonical test case of inviscid homogeneous decaying turbulence in a periodic cube at Mach 0.1. Figure 2 shows the turbulent kinetic energy spectra. There is a large improvement with the proposed modification, showing a significant $k^{-5/3}$ subinertial range. Note that the fifth-order method is already a significant improvement on second-order MUSCL methods such as van Leer, van Albada, and minmod extrapolations. The spectral accuracy, defined as the ratio of the magnitude of the shock-capturing fluxes F_{sc} over the spectral fluxes F_{spectral} [28,35], is shown in Fig. 3, in which a value of 1 indicates spectral accuracy. This demonstrates that the modified scheme maintains spectral accuracy to a higher wave number than the standard ninth-order WENO of Balsara and Shu [34], at a computational cost only 20% greater than the van Leer limiter.

Finally, a third-order-accurate Runge–Kutta time-stepping method is employed [36]:

$$U_i^1 = U_i^n + \frac{1}{2}\frac{\delta t}{\delta x} f(U_i^n) \tag{16}$$

$$U_i^2 = U_i^n + \frac{1}{2}\frac{\delta t}{\delta x}[f(U_i^1)] \tag{17}$$

$$U_i^{n+1} = \frac{1}{3}\left(2U_i^2 + U_i^n + \frac{\delta t}{\delta x}[f(U_i^2) + f(U_i^1)]\right) \tag{18}$$

where $f(U_i^n)$ indicates the net flux into the cell evaluated using the array of conserved variables at time n in cell position i (see also Drikakis and Rider [13]). This has an extended stability region to a theoretical Courant–Friedrichs–Lewy number of 2.

C. Grid, Boundary Conditions, and Initial Conditions

The grid size follows that of Larcheveque et al. [6] and takes the dimensions shown in Fig. 1. The origin of the chosen coordinate system is on the upstream bottom corner of the cavity, in which positive x is in the direction of the mean flow, positive z is vertical in

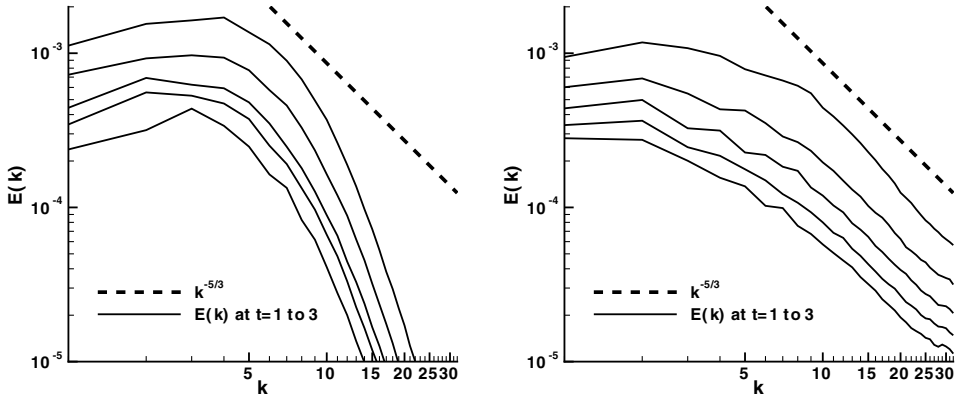

Fig. 2 Turbulent kinetic energy spectra for homogeneous decaying turbulence at 64^3 for the original fifth-order method (left) and modified scheme (right).

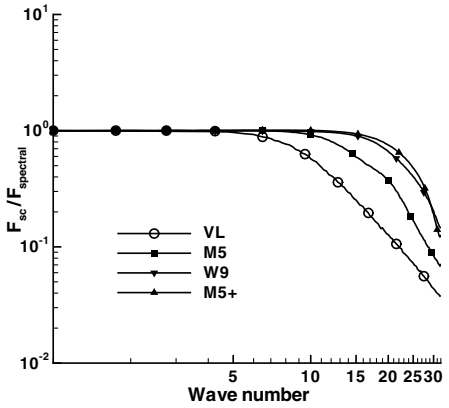

Fig. 3 Spectral accuracy of the modified scheme compared with second-order van Leer (VL) and ninth-order WENO (W9).

the wind tunnel, and y is the width of the domain, chosen as 0.05 m. Three different grid sizes were employed, consisting of 0.8×10^6, 1.4×10^6, and 3×10^6 cells for the coarse, medium, and fine simulations, respectively.

It is not considered that the development of the shear layer over the cavity is sensitive to the exact nature of the turbulent boundary layer. Hence, although the simulation is greatly underresolved (even at the finest grid level $y^+ \approx 20$, the medium and coarse grids have y^+ of 42 and 55, respectively), no turbulent-wall model was employed, and the walls of the wind tunnel were modeled as nonslip. Inlet boundary conditions were fixed assuming isentropic expansion from the experimental reservoir conditions ($p_0 = 98000$ Pa and $T_0 = 293$ K) to Mach 0.8. This gives a pressure of 64,304 Pa, density of 0.8623 kg/m^3, and a velocity equal to 258 m/s. The experiment measured turbulent noise levels of 1.5% of the freestream velocity; however, numerical tests with imposed white noise on the inlet boundary condition up to 15% of the freestream velocity showed no significant influence on the flow physics of the separated mixing layer.

The boundary layer at the inlet is defined using the experimentally measured incompressible shape factor and momentum thickness to define the power-law profile. Hence, for $y/\delta < 1$,

$$\langle U \rangle = U\left(\frac{y}{\delta}\right)^{1/n} \tag{19}$$

where $n = 2/(H-1)$ is determined from the incompressible shape factor $H = 1.3$, and δ is determined using the momentum thickness $\theta = 0.65$ mm:

$$\delta = \frac{\theta(n+1)(n+2)}{n} \tag{20}$$

The exit boundary condition is extrapolated from the internal flow. Because the flow is subsonic, this condition is not rigorous as there are waves propagating upstream; however, a strong grid stretching in the x direction damps acoustic perturbations far downstream of the

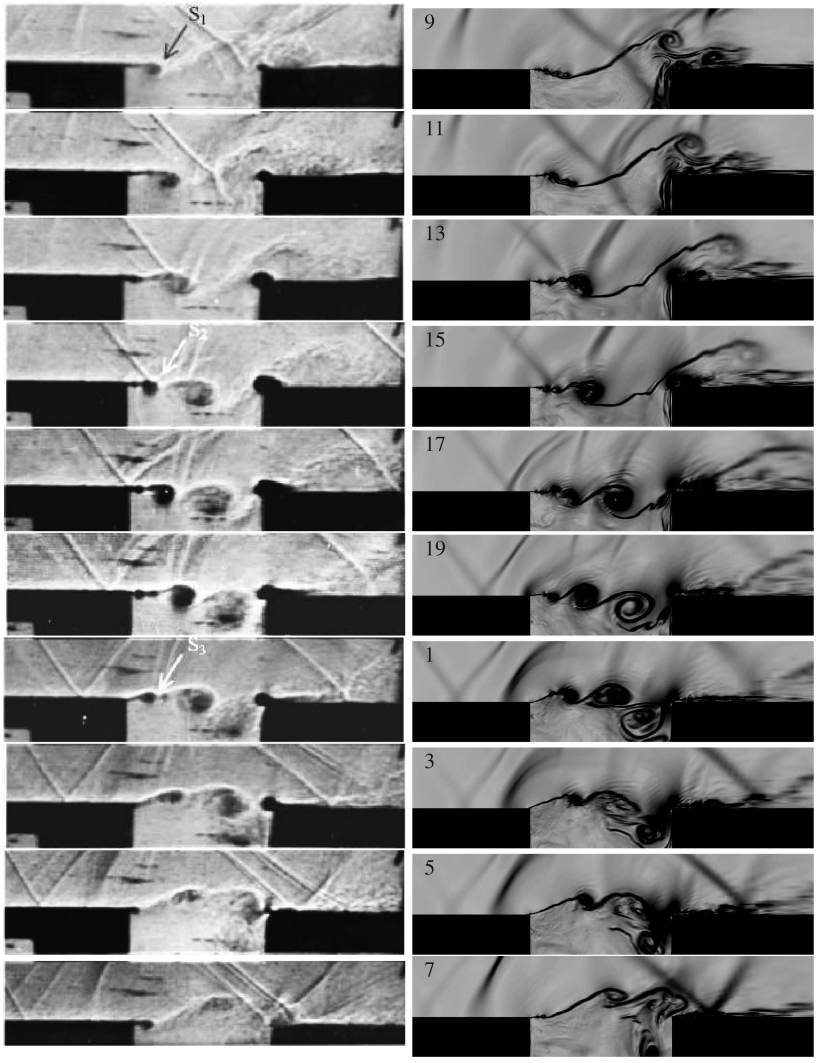

Fig. 4 Comparison of experimental schlieren images (left) and computational schlieren $|\nabla\rho|$ (right) at approximately the same time within the vortex-shedding cycle. The experimental images are reproduced from Forestier et al. [5].

cavity. The constant-velocity flowfield is maintained by a pressure drop that is imposed on the initial condition, aimed to compensate for momentum losses due to viscous drag at the wall and losses due to the cavity. Assuming that the losses in the boundary layer are similar to those over a flat plate, the shear stress can be estimated from the empirical relation [37]

$$\tau_w = \tfrac{1}{2}\rho U^2 C_f, \qquad C_f = 0.074/Re^{0.2} \tag{21}$$

and the required pressure drop is given by

$$\Delta p = 2\tau_w A_{xy}/A_{yz} \tag{22}$$

where A_{xy} is the area of the top and bottom walls, and A_{yz} is the cross-sectional area of the domain. The mean flow is 258 m/s and the ratio of areas is 3, giving $\tau_w = 32$ Pa and an imposed pressure drop of $\Delta p = 198$ Pa. This pressure drop is imposed linearly throughout the domain at initialization.

III. Results and Discussion

A. Flow Phenomenology

High-speed schlieren images taken during the experiment demonstrated that the mixing layer undergoes a clear periodic cycle. This cycle is illustrated in Fig. 4, which compares experimental schlieren images (reproduced from Fig. 2 of Forestier et al. [5]) and computational schlieren results on the finest grid level ($|\nabla\rho|$). The first vortex (labeled S_1 on the experimental images) forms in which the boundary layer separates from the upstream edge of the cavity. It then grows rapidly in size and propagates downstream. At the same time, the second structure (labeled S_2) begins to form at the separation point. At phase number 13 in the sequence, there is a strong shock–vortex interaction, resulting in deformation of the acoustic wave as it passes through the leading vortical structure. This releases a cylindrical sound wave as the vortex core is compressed into an elliptical shape during the passage of the wave, releasing acoustic waves as it returns to circular shape (these can be seen at phase numbers 15 and 17).

The third vortex is visible at phase 19, at which time the first vortex is approaching the downstream wall and is deflected downward. Because the first vortex is strong, as it is shifted down the wall it induces an upward velocity on the developing second and third vortical structures, lifting them. In the final few images, the second vortical structure strikes the downstream corner of the cavity, whereas the third vortex is lifted over the edge and continues downstream. The sequence of vortex shedding is broken by a strong pressure wave that reflects from the bottom of the cavity, cutting the shedding process close to the upstream corner of the cavity. This pressure wave can be seen passing the upstream corner in images at phase numbers 19 to 7 in Fig. 4.

Acoustic waves are generated as the vortices impact on the downstream corner and they propagate upstream and downstream, and in an additional complexity, they are reflected off the top of the wind tunnel. These waves are seen clearly in the experimental and numerical images; however, in the numerical images, the reflected acoustic waves (leaning toward the upstream direction) are not as sharp, due to grid stretching at the upper boundary. The prediction of the location of the acoustic waves is excellent when compared with experimental images. The network of emitted and reflected waves can be seen clearly in Fig. 5, which shows the full computational domain.

Figures 6 and 7 show a three-dimensional view of the vortices, visualized as isosurfaces Q criteria [38]

$$Q = -\frac{1}{2}\frac{\partial u_i}{\partial x_j}\frac{\partial u_j}{\partial x_i} \tag{23}$$

demonstrating the complexity of the flow close to the shear layer. It also illustrates the dampening effect of grid stretching both at the bottom of the cavity and in the boundary layer downstream of the cavity. Figure 7 shows the isosurfaces of $Q = 0.5 \times 10^6$, half the value taken for Fig. 6 to illustrate the complex three-dimensional

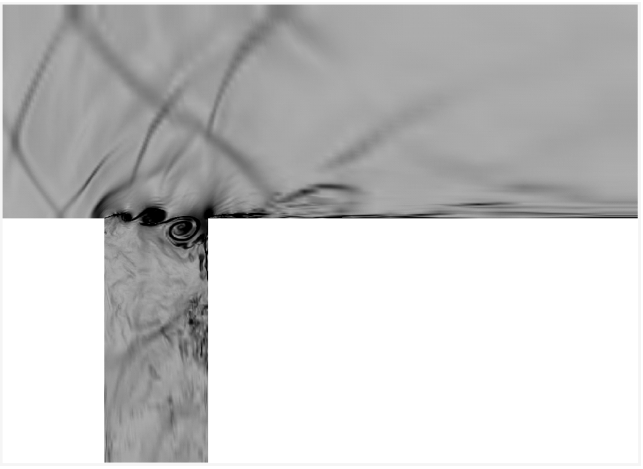

Fig. 5 Computational schlieren $|\nabla\rho|$ showing the full computational domain at the finest grid resolution.

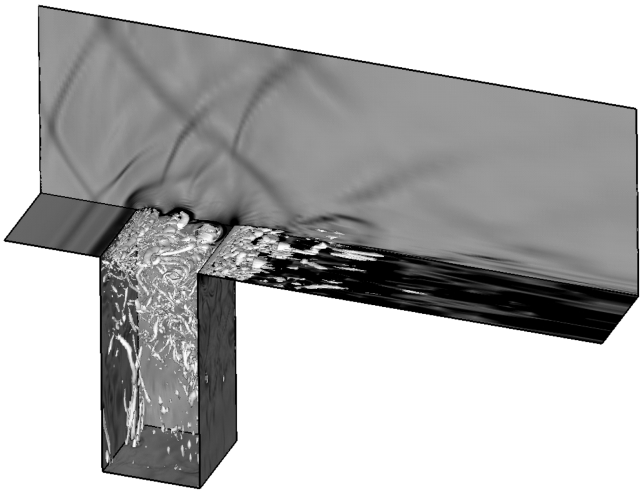

Fig. 6 Three-dimensional visualization of isosurfaces of $Q = 10^6$ at the same time as Fig. 5. The contour flood shows a pseudoschlieren field ($|\nabla\rho|$).

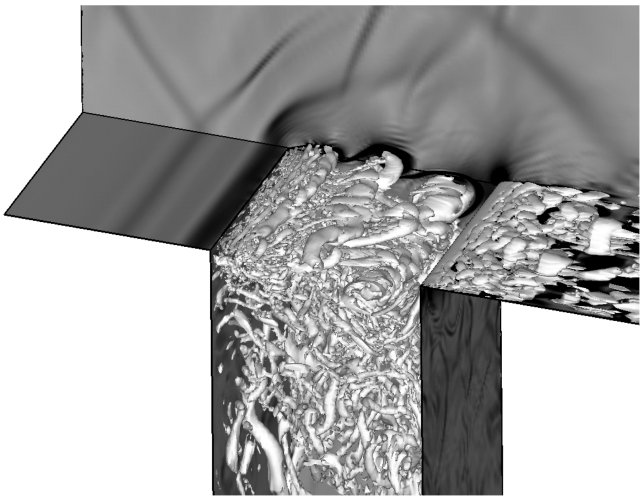

Fig. 7 Close-up of the cavity showing visualization of isosurfaces of $Q = 0.5 \times 10^6$ at the same time as Fig. 6, but with an isosurface at half the value. The contour flood shows pseudoschlieren field ($|\nabla\rho|$).

turbulent nature of the flow. The mixing layer is dominated by the three quasi-two-dimensional vortices; however, between these vortices are smaller streamwise vortices. There is also evidence that finer-scale vortices, resulting from turbulent motion within the cavity, are subsequently entrained into the mixing layer.

B. Mean Flow

The Reynolds-averaged mean flow data were computed from data outputted for approximately 30 shedding cycles for the coarse and fine data and 60 shedding cycles for the medium-resolution simulation. The results are presented in Figs. 8 and 9, compared with experimental data measured using laser Doppler velocimetry along the developing mixing layer for several thousand shedding cycles and with the fine-grid results from the LES study by Larcheveque et al. [6].

The overall agreement with experiment is excellent, especially considering the minimal approach to modeling the incoming boundary layers and strong grid stretching at the upper wall. Comparing the results at $x/l = 0.05$, it appears that the initialized boundary layer at the inlet of the numerical domain is slightly thicker than required. There is a u-momentum loss between $z/L = 2.4$ and 2.5 when compared with the experimental results, which in turn causes the center of the mixing layer to be slightly higher.

The agreement at subsequent points is excellent; the only slight discrepancy is a consistent underestimation of the u velocity above the cavity, which is due to the initial thickness of the upstream boundary layer. There are discrepancies close to the downstream

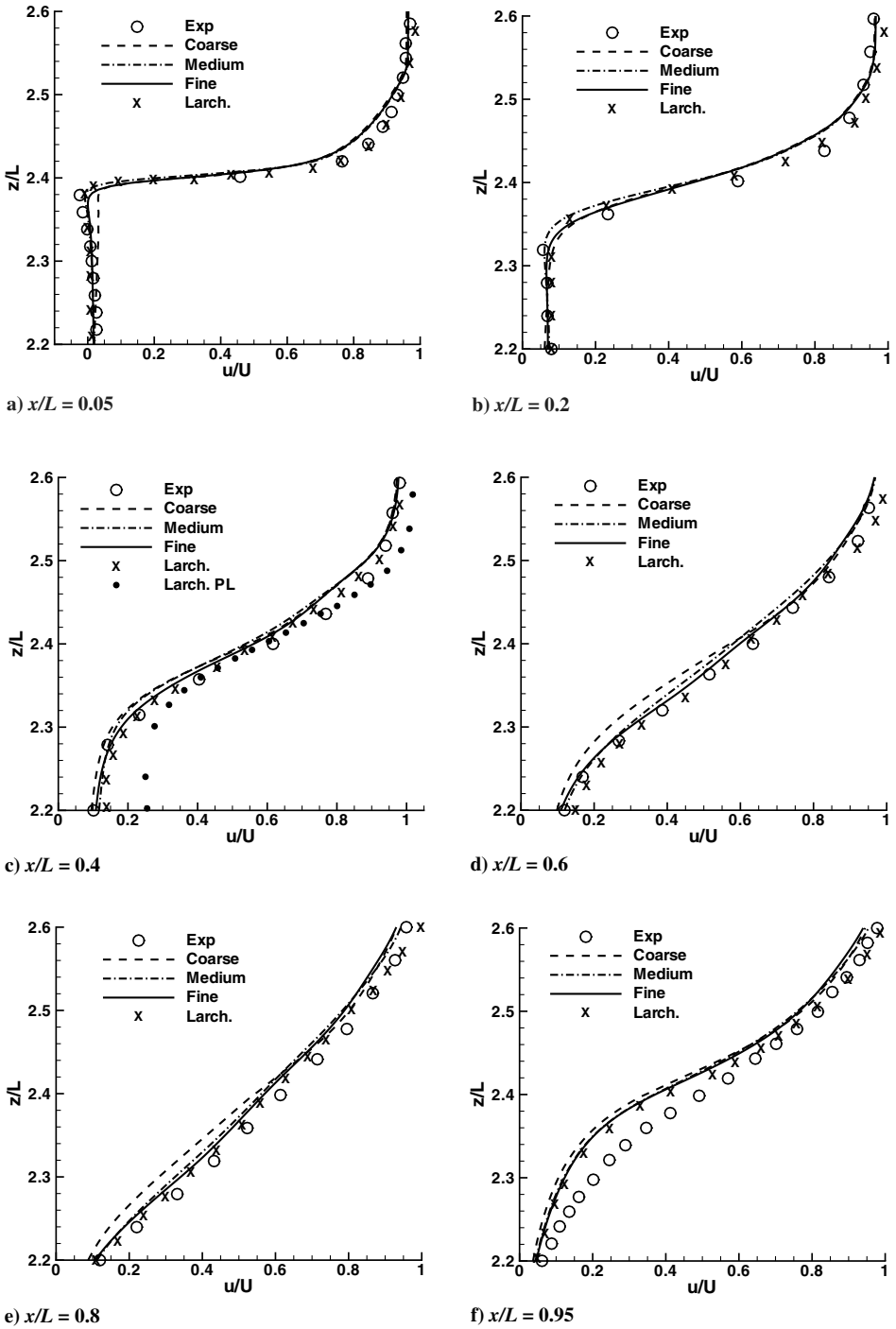

Fig. 8 Comparison of mean longitudinal velocity $\bar{u}/U$ with the experiment and previous LES [6]. For $x/L = 0.4$ the results from [6] gained using a power-law boundary-layer profile are plotted with solid circles.

edge of the cavity wall, however: in this region, there is a complex fine-scale interaction between the developing vortices and the downstream wall that is not well resolved.

The vertical velocities presented in Fig. 9 are approximately 1 order of magnitude smaller than the freestream velocity. At the first measurement station $x/L = 0.05$, the mean velocities are extremely well predicted on the fine grid; however, the peak velocities in the center of the layer are not predicted as accurately as in the other locations. At the other locations, both the qualitative and quantitative behavior are captured well, indicating that the mixing layer is growing in a physically realistic manner.

At the majority of measurement planes, there is a clear trend in improvement as resolution increases, converging toward the experimental measurements.

Comparison with the previous LES of Larcheveque et al. [6] shows that on equivalent grids (medium grid in the current study with fine in the Larcheveque et al. case), the agreement with experiment is not as good for the longitudinal velocities, but is as good for the vertical velocities. The key difference between the two simulations is visible in Fig. 8a). The inlet boundary-layer profile used by Larcheveque et al. was not that reported by Forestier et al. [5], but a least-squares fit to their experimental data. This was then rescaled to allow for growth up to the start of the cavity to give the best match to experimental data at $x/L = 0.4$, in conjunction with turbulent-wall modeling. The simulations detailed here initialized the inlet boundary-layer profile directly from experimental measurements without such compensation, which meant that the initial boundary-layer thickness is slightly larger than that in the computation. This is a point that should be improved in future simulations.

To support this conclusion, the solid circles in Fig. 8c show the results gained by Larcheveque et al. [6] using ILES on a grid equivalent to the coarse grid employed here, but with a power-law

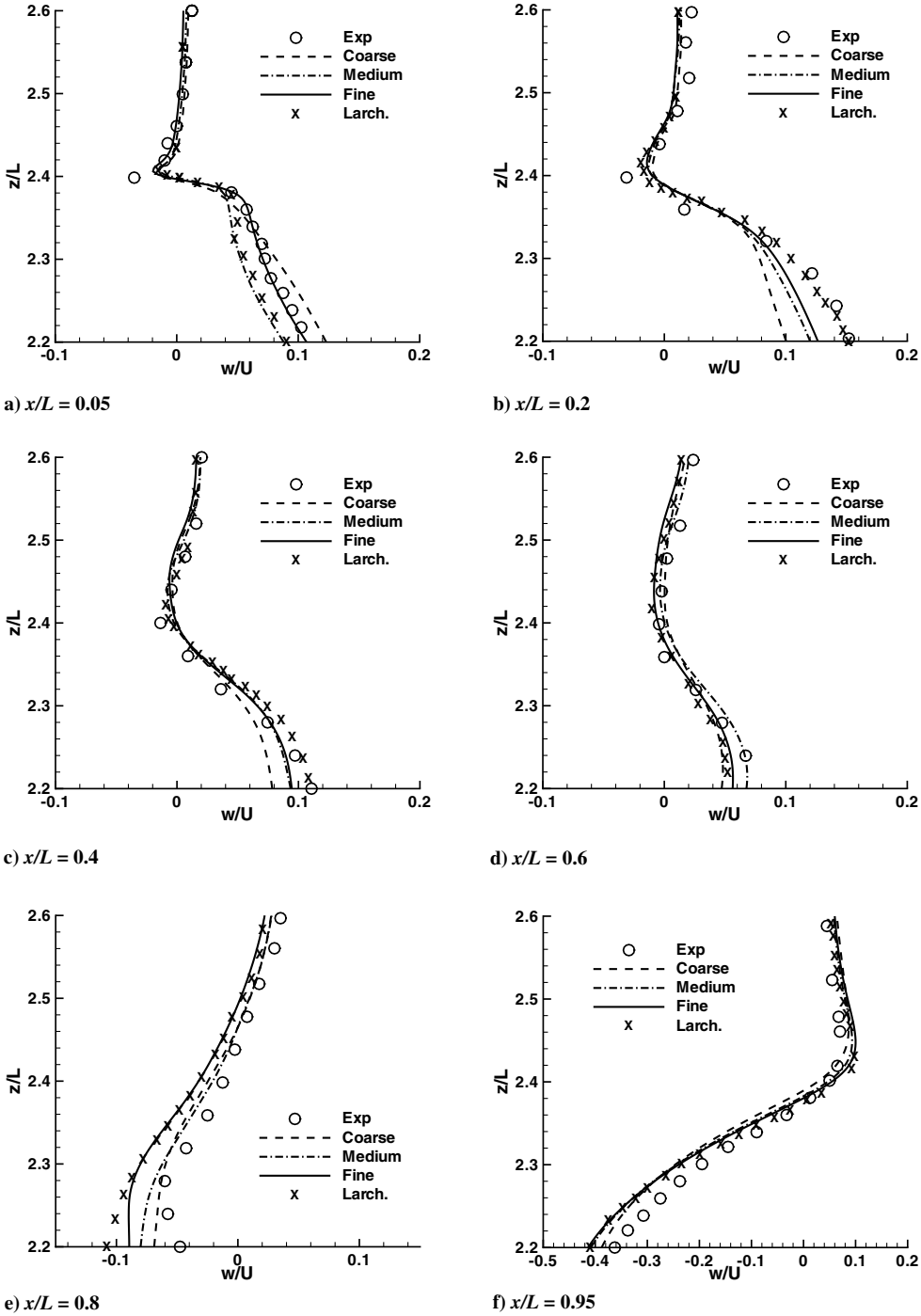

Fig. 9 Comparison of mean longitudinal velocity $\bar{w}/U$ with experiment and previous LES [6].

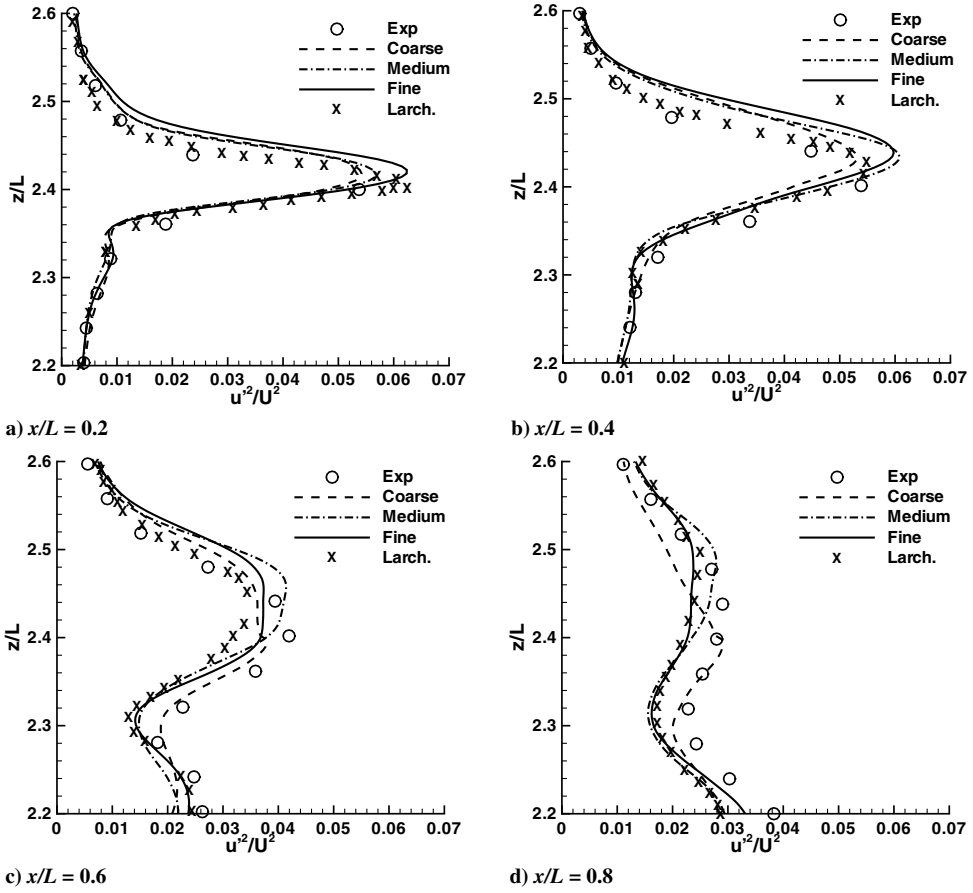

Fig. 10 Comparison of $\bar{u}'^2/U$ with experiment and previous LES [6].

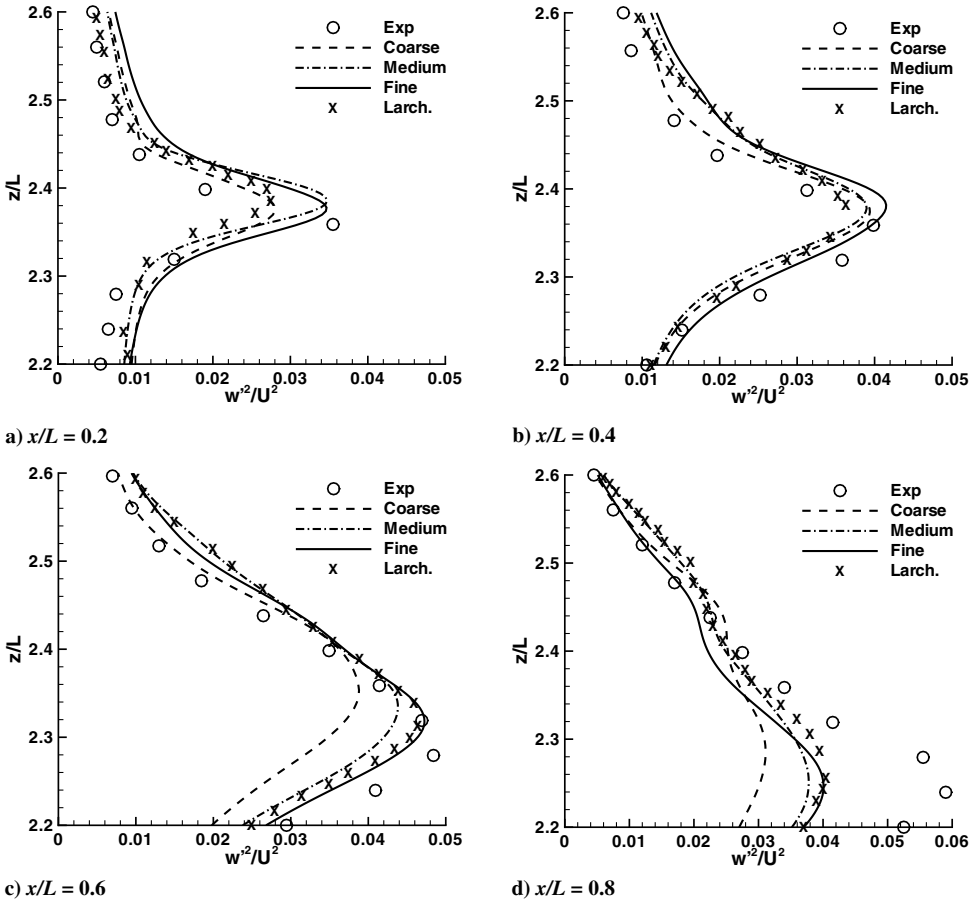

Fig. 11 Comparison of $\bar{w}'^2/U$ at with experiment and previous LES [6].

inlet boundary condition for the turbulent boundary layer. This is the same type of inlet boundary condition employed in the current simulations, but the results are substantially worse. This indicates that, to some extent, the ILES results presented here are less sensitive to the initial modeling assumptions and that the proposed numerical method gives a better representation of the expected flow physics.

C. Reynolds Stresses

The time and space (in the periodic direction) averaged longitudinal Reynolds stresses are plotted against the experiment in Fig. 10. As with the mean flow velocities, there is good agreement with experimental results at all stations. The center of the mixing layer in the numerical simulations is slightly higher than that in the experiment (see Figs. 10a and 10b), which is consistent with a thicker boundary layer upstream of the cavity.

The vertical Reynolds stress $\bar{w}'^2/U$ plotted in Fig. 11 shows similar results to the longitudinal stresses. The peak of the vertical Reynolds stress indicates that the center of the developing mixing layer is too high by about 1 mm in comparison with experimental results. The cross stress $\overline{u'w'}/U$ presented in Fig. 12 also confirms this observation.

Finally, Fig. 13 shows the two-dimensional fluctuating kinetic energy close to the upstream and downstream walls, respectively. There is a slight overestimation of the turbulent kinetic energy at all grid resolutions, which is opposite to the results presented by [6], in which conventional LES underestimated the fluctuating kinetic energy. This demonstrates that the numerical scheme is suitable for LES, because it does not excessively damp turbulent motions.

At this point, it is worth discussing the relative modeling effort in the classical and ILES simulations and the properties of the numerical schemes. The subgrid model employed by Larcheveque et al. [6] is a selective mixed-scale model, described in detail by Lenormand et al. [39]. This uses a nonlinear combination of a Smagorinsky and mixing-length model. It requires the choice of two

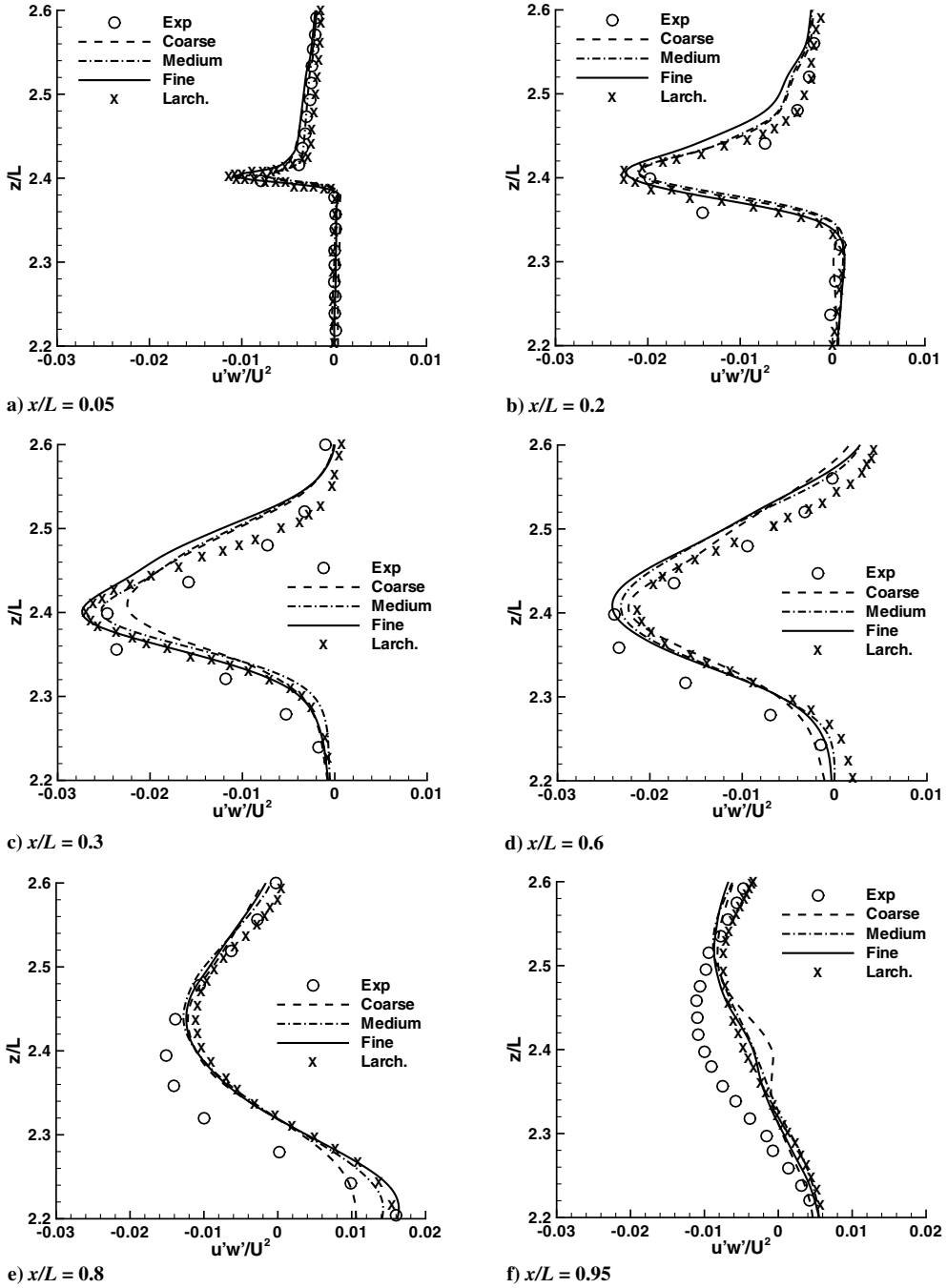

Fig. 12 Comparison of $\overline{u'w'}/U$ with experiment and previous LES [6].

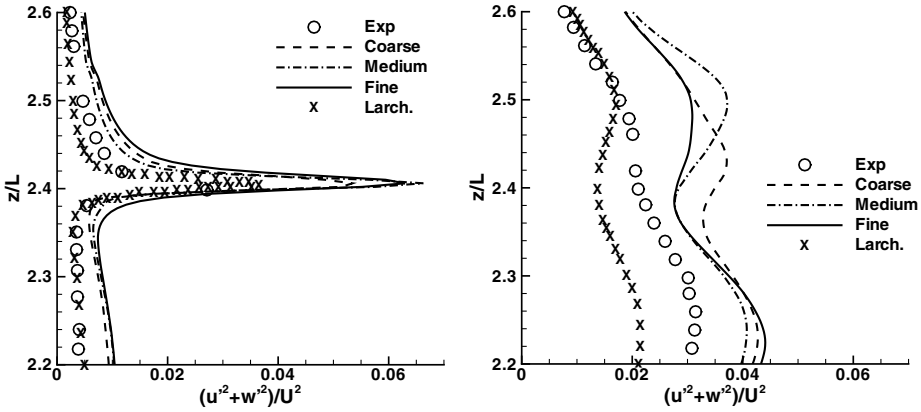

Fig. 13 Comparison of $(\bar{u}'^2 + \bar{w}'^2)/U^2$ with experiment and previous LES [6].

constants: the Smagorinsky coefficient and the nonlinear combination parameter. In addition, the Smagorinsky coefficient is modified for use in the mixing-length model close to walls via the van Driest dampening function. To improve intermittency, an additional selective function is employed that premultiplies the eddy viscosity computed via the subgrid models. A further correction is employed for the filter length Δ to compensate for the fact that the mesh is highly stretched. Finally, the subgrid models themselves are evaluated numerically to second-order accuracy. The Smagorinsky coefficient, the nonlinear combination parameter, and the selective function are all calibrated through comparison of numerical results with the experiment [39]. The underlying numerical method is a combination of a second-order central-difference scheme with dissipation added to stabilize the numerical scheme by upwinding in which oscillations occur. The numerical scheme is not shock-capturing, due to this oscillatory nature.

In contrast, the ILES approach appears very stark. No explicit subgrid models were employed, correction functions are not necessary, and the scheme is shock-capturing, as demonstrated by Thornber et al. [8]. However, it is clear that a turbulent-wall model (or improved inlet conditions) should be implemented in future simulations, because the results in this section have demonstrated that there is some sensitivity to the details of the incoming boundary-layer profile on the location of the center of the mixing layer and the exact match with the experiment.

D. Pressure Spectra

In the experiment, the average pressure power spectrum was measured at the upstream wall over approximately 5000 to 8000 shedding periods. Because the time simulated is limited by computational power, the results presented within this section

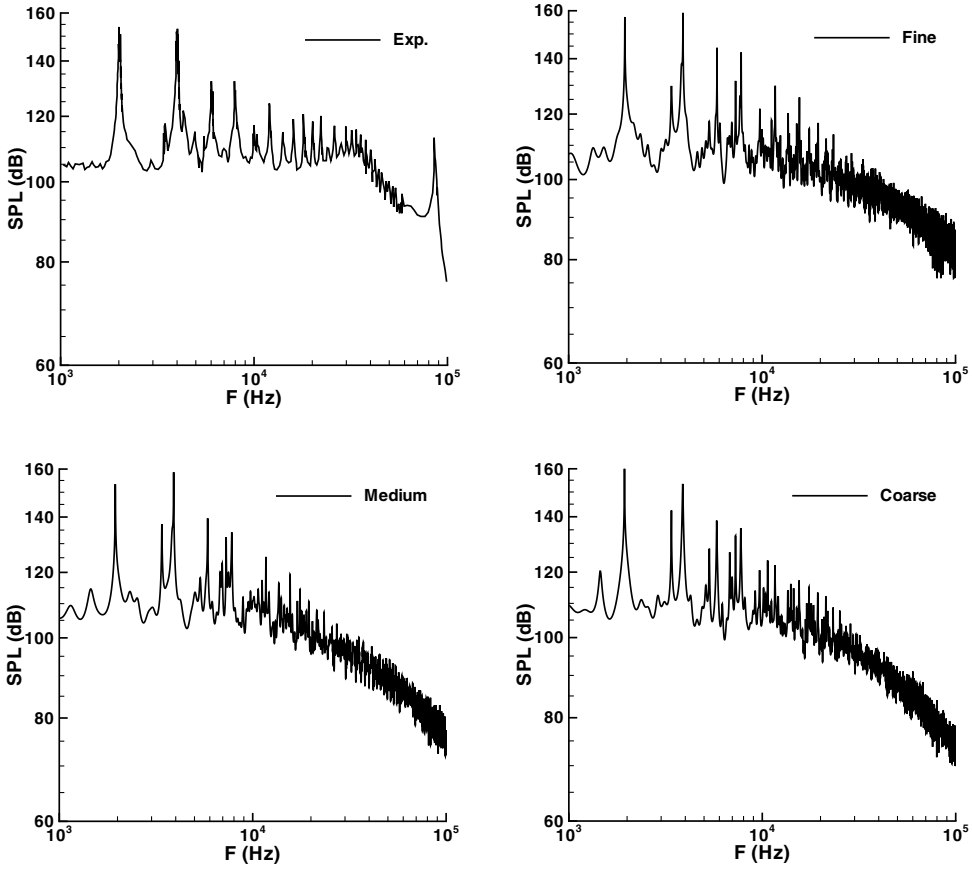

Fig. 14 Pressure power spectrum up to 10 kHz for simulations and experiment.

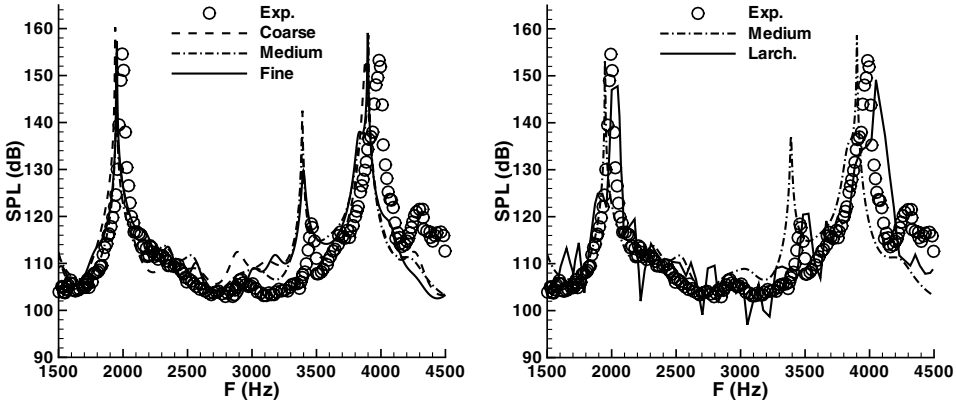

Fig. 15 Pressure power spectrum highlighting the dominant acoustic modes for the ILES simulations (left) and comparison of the fine-grid results using conventional LES [6].

correspond to 30 shedding periods. To examine the influence of sampling time, the medium-grid level was run for 60 shedding periods. All pressure spectra are presented as frequency vs sound pressure level (SPL) in units of decibels (dB), where the conversion to decibel is

$$\text{SPL (dB)} = 10\log_{10}\left(\frac{\text{power}}{4\times 10^{-10}}\right) \tag{24}$$

Burg's method (also known as the minimum entropy method) is employed to compute the spectra, which does not employ an explicit Fourier transform. This employs linear prediction theory, which was initially developed for predicting the value of a function at one instant using a combination of all previous instants. The coefficients of the linear prediction can be directly related to the power spectrum of the function; they provide an excellent method of extracting sharp peaks from short data samples and do not rely on a data set that is a power of 2 in length.

Figure 14 shows the pressure power spectrum for each of the three grid resolutions and that of the experiment for the full range. A close-up of the first two peaks is shown in Fig. 15, comparing the different methods. It should be noted that the peak in the experimental results at about 90 kHz is believed to be due to resonance of the sensor itself. Experimental measurements recorded the fundamental mode at 1975 Hz (no error bars are given by Forestier et al. [5]) at an approximately 155-dB sound pressure level. The coarse, medium, and fine grids predict this peak at 1940, 1948, and 1954 Hz, with a sound pressure level of 160, 153, and 157 dB, respectively. This is equivalent to errors compared with the experiment of less than 5 dB at all grid levels. These are excellent results considering that the boundary layers were not modeled and that extremely coarse grids were used in the upper half of the wind tunnel and bottom of the cavity.

As can be seen in Fig. 15, the frequency of the second mode is also predicted to within 2%, but the sound pressure level is overestimated by 6 dB at the highest grid level. Additionally, the small peak between the first two modes is overestimated significantly; however, because the scale is logarithmic, this would not affect total sound pressure significantly. The source of the smaller peak is a longitudinal wave that is reflected continuously within the cavity. This wave is stronger in the simulation than in the experiment. A possible explanation is that in the experiment, the acoustic wave is scattered by a series of interactions with turbulent vortices. The coarse resolution in the numerical simulation means that the vortices are not present, and hence the acoustic waves are not scattered as effectively.

Figure 15 also shows a comparison of the medium-grid simulation with the fine-grid results of Larcheveque et al. [6]. The prediction from the medium-grid simulation of the current study is a better match to experimental data for the location and magnitude of the two strongest modes; however, the conventional LES simulation captures the magnitude of the small peak better. It is possible that the combination of a two- and three-dimensional grid in the conventional LES simulation allowed better resolution of the flow within the cavity in which the acoustic waves producing the small peak occur. It is expected that the shock-capturing capability of the current method allows better resolution of strong acoustic waves (weak shocks), which appears to be confirmed here.

Comparing the full range, the fine-grid level predicts the frequency of the harmonics up to approximately 20 kHz (the first 11 modes); however, the magnitude of the higher-frequency peaks are overestimated compared with the experiment. The medium grid performs better in terms of magnitude of the harmonics, but resolves up to about 15 kHz (first 8 modes). The coarse mesh captures modes up to 12 kHz; however, there are several spurious peaks at high frequency that do not appear in the experimental results. In all, the agreement with experimental sound pressure spectra is excellent.

IV. Conclusions

A comparison between implicit large-eddy simulation, large-eddy simulation with a selective mixed-scale model, and experimental results for a deep open cavity flow was presented. It was shown that the mean flow and Reynolds stresses are in very good agreement with the experiment, and convergence toward the experimental results with increasing resolution is apparent.

The numerical pressure power spectra predict the frequency of the two dominant modes to within 2% and the sound pressure level within 6 dB for all grid resolutions. The finest grid level captures the frequency of harmonics up to 20 kHz; however, the magnitude of these peaks is overestimated. Results presented with the modified method without subgrid model compare excellently with conventional large-eddy simulation.

In summary, this paper has validated the modified numerical scheme through simulations of a complex wall-bounded compressible turbulent flow. The comparison shows excellent results for minimum modeling effort and demonstrates that the key flow physics of the problem are captured accurately without the necessity of an explicit subgrid model.

Acknowledgments

The computations were carried out on the Cranfield High Performance Computing Facility and the United Kingdom's National Supercomputer (HPCx) through the Engineering and Physical Sciences Research Council (EPSRC) grant "Proposal for HPCx Resources and Support for the LESUK3 Consortium" (EP/D053994/1).

References

[1] Rossiter, J., "Wind-Tunnel Experiments on the Flow Over Rectangular Cavities at Subsonic and Transonic Speeds," Aerospace Research Council, Reports and Memoranda No. 3438, London, 1964.

[2] Langtry, R., and Spalart, P., "DES Investigation of a Baffle Device for Reducing Landing-Gear Cavity Noise," AIAA Paper 2008-13, Jan. 2008.

[3] Rowley, C., Juttijadata, V., and Williams, D., "Cavity Flow Control Simulations and Experiments," AIAA Paper 2005-0292, Jan 2005.
[4] Kim, C-K., Yu, S.-T. J., and Zhang, Z.-C., "Cavity Flow in Scramjet Engine by Space-Time Conservation and Solution Element Method," *AIAA Journal*, Vol. 42, No. 5, May 2004, pp. 912–919.
[5] Forestier, N., Jacquin, L., and Geffroy, P., "The Mixing Layer over a Deep Cavity at High-Subsonic Speed," *Journal of Fluid Mechanics*, Vol. 475, 2003, pp. 101–144. doi:10.1017/S0022112002002537
[6] Larcheveque, L., Sagaut, P., Mary, I., and Labbe, O., "Large-Eddy Simulation of a Compressible Flow Past a Deep Cavity," *Physics of Fluids*, Vol. 15, No. 1, 2003, pp. 193–209. doi:10.1063/1.1522379
[7] Thornber, B., Drikakis, D., and Williams, R., "On Entropy Generation and Dissipation of Kinetic Energy in High-Resolution Shock-Capturing Schemes," *Journal of Computational Physics*, Vol. 227, No. 10, 2008, pp. 4853–4872. doi:10.1016/j.jcp.2008.01.035
[8] Thornber, B., Mosedale, A., Drikakis, D., Youngs, D., and Williams, R., "An Improved Reconstruction Method for Compressible Flows with Low Mach Number Features," *Journal of Computational Physics*, Vol. 227, No. 10, 2008, pp. 4873–4894. doi:10.1016/j.jcp.2008.01.036
[9] Boris, J., Grinstein, F., Oran, E., and Kolbe, R., "New Insights into Large Eddy Simulation," *Fluid Dynamics Research*, Vol. 10, Nos. 4–6, 1992, pp. 199–228. doi:10.1016/0169-5983(92)90023-P
[10] Youngs, D., "Three-Dimensional Numerical Simulation of Turbulent Mixing by Rayleigh-Taylor Instability," *Physics of Fluids A*, Vol. 3, No. 5, 1991, pp. 1312–1320. doi:10.1063/1.858059
[11] Fureby, C., Tabor, F., Weller, H., and Gosman, A., "A Comparative Study of Subgrid Scale Models in Homogeneous Isotropic Turbulence," *Physics of Fluids*, Vol. 9, No. 5, 1997, pp. 1416–1429. doi:10.1063/1.869254
[12] Jimenez, J., Wray, A., Saffman, P., and Rogallo, R., "The Structure of Intense Vorticity in Isotropic Turbulence," *Journal of Fluid Mechanics*, Vol. 255, No. 1, 1993, pp. 65–90. doi:10.1017/S0022112093002393
[13] Drikakis, D., and Rider, W., *High-Resolution Methods for Incompressible and Low-Speed Flows*, Springer-Verlag, New York, 2004.
[14] Grinstein, F., Margolin, L., and Rider, W. (eds.), *Implicit Large Eddy Simulation: Computing Turbulent Fluid Dynamics*, Cambridge Univ. Press, Cambridge, England, U.K., 2007.
[15] Youngs, D., "Application of MILES to Rayleigh-Taylor and Richtmyer-Meshkov Mixing," AIAA Paper 2003-4102, June 2003.
[16] Thornber, B., Youngs, D., and Drikakis, D., "High Resolution Methods for Planar 3D Richtmyer-Meshkov Instabilities," 10th International Workshop on the Physics of Compressible Turbulent Mixing, Commissariat a l'Energie Atomique Paper 21, July 2006.
[17] Grinstein, F., and Fureby, C., "Recent Progress on MILES for High Reynolds Number Flows," *Journal of Fluids Engineering*, Vol. 124, No. 4, 2002, pp. 848–861. doi:10.1115/1.1516576
[18] Hahn, M., and Drikakis, D., "Large Eddy Simulation of Compressible Turbulence Using High-Resolution Methods," *International Journal for Numerical Methods in Fluids*, Vol. 47, Nos. 8–9, 2005, pp. 971–977. doi:10.1002/fld.882
[19] Drikakis, D., "Advances in Turbulent Flow Computations Using High-Resolution Methods," *Progress in Aerospace Sciences*, Vol. 39, Nos. 6–7, 2003, pp. 405–424. doi:10.1016/S0376-0421(03)00075-7
[20] Margolin, L., Smolarkiewicz, P., and Sorbjan, Z., "Large-Eddy Simulations of Convective Boundary Layers Using Nonoscillatory Differencing," *Physica D*, Vol. 133, 1999, pp. 390–397. doi:10.1016/S0167-2789(99)00083-4
[21] Smolarkiewicz, P., and Margolin, L., "Mpdata: A Finite Difference Solver for Geophysical Flows," *Journal of Computational Physics*, Vol. 140, No. 2, 1998, pp. 459–480. doi:10.1006/jcph.1998.5901
[22] Gordnier, R., and Visbal, M., "Compact Difference Scheme Applied to Simulation of Low-Sweep Delta Wing Flow," *AIAA Journal*, Vol. 43, No. 8, 2005, pp. 1744–1752. doi:10.2514/1.5403
[23] Drikakis, D., Fureby, C., Grinstein, F., Hahn, M., and Youngs, D., "MILES of Transition to Turbulence in the Taylor-Green Vortex System," *ERCOFTAC Workshop on Direct and Large Eddy Simulation-6*, Springer, Dordrecht, The Netherlands, Sept. 2006, pp. 159–166.
[24] Porter, D., Woodward, P., and Pouquet, A., "Inertial Range Structures in Decaying Compressible Turbulent Flows," *Physics of Fluids*, Vol. 10, No. 1, 1998, pp. 237–245. doi:10.1063/1.869563
[25] Fureby, C., and Grinstein, F., "Large Eddy Simulation of High-Reynolds-Number Free and Wall-Bounded Flows," *Journal of Computational Physics*, Vol. 181, No. 1, 2002, pp. 68–97. doi:10.1006/jcph.2002.7119
[26] Margolin, L., Smolarkiewicz, P., and Wyszogrodzki, A., "Implicit Turbulence Modelling for High Reynolds Number Flows," *Journal of Fluids Engineering*, Vol. 124, No. 4, 2002, pp. 862–867. doi:10.1115/1.1514210
[27] Hickel, S., Adams, N., and Domaradzki, J., "An Adaptive Local Deconvolution Method for Implict LES," *Journal of Computational Physics*, Vol. 213, No. 1, 2006, pp. 413–436. doi:10.1016/j.jcp.2005.08.017
[28] Thornber, B., Mosedale, A., and Drikakis, D., "On the Implicit Large Eddy Simulation of Homogeneous Decaying Turbulence," *Journal of Computational Physics*, Vol. 226, No. 2, 2007, pp. 1902–1929. doi:10.1016/j.jcp.2007.06.030
[29] Toro, E., *Riemann Solvers and Numerical Methods for Fluid Dynamics*, Springer–Verlag, New York, 1997.
[30] Van Leer, B., "Towards the Ultimate Conservative Difference Scheme, 4: A New Approach to Numerical Convection," *Journal of Computational Physics*, Vol. 23, No. 3, 1977, pp. 276–299. doi:10.1016/0021-9991(77)90095-X
[31] Kim, K., and Kim, C., "Accurate, Efficient and Monotonic Numerical Methods for Multi-Dimensional Compressible Flows Part 2: Multi-Dimensional Limiting Process," *Journal of Computational Physics*, Vol. 208, No. 2, 2005, pp. 570–615. doi:10.1016/j.jcp.2005.02.022
[32] Volpe, G., "Performance of Compressible Flow Codes at Low Mach Number," *AIAA Journal*, Vol. 31, No. 1, 1993, pp. 49–56. doi:10.2514/3.11317
[33] Kolmogorov, A., "The Local Structure of Turbulence in an Incompressible Fluid at Very High Reynolds Numbers," *Doklady Akademii Nauk SSSR*, Vol. 30, 1941, p. 299.
[34] Balsara, D., and Shu, C.-W., "Monotonicity Preserving Weighted Essentially Nonoscillatory Schemes with Increasingly High Order of Accuracy," *Journal of Computational Physics*, Vol. 160, No. 2, 2000, pp. 405–452. doi:10.1006/jcph.2000.6443
[35] Garnier, E., Mossi, M., Sagaut, P., Comte, P., and Deville, M., "On the Use of Shock-Capturing Schemes for Large-Eddy Simulation," *Journal of Computational Physics*, Vol. 153, No. 2, 1999, pp. 273–311. doi:10.1006/jcph.1999.6268
[36] Spiteri, R., and Ruuth, S., "A Class of Optimal High-Order Strong-Stability Preserving Time Discretization Methods," *SIAM Journal on Numerical Analysis*, Vol. 40, No. 2, 2002, pp. 469–491. doi:10.1137/S0036142901389025
[37] Anderson, J., *Fundamentals of Aerodynamics*, McGraw–Hill, New York, 2001.
[38] Jeong, J., and Hussain, F., "On the Identification of a Vortex," *Journal of Fluid Mechanics*, Vol. 285, 1995, pp. 69–94. doi:10.1017/S0022112095000462
[39] Lenormand, E., Sagaut, P., Phuoc, L., and Comte, P., "Subgrid-Scale Models for Large-Eddy Simulation of Compressible Wall Bounded Flows," *AIAA Journal*, Vol. 38, No. 8, 2000, pp. 1340–1350.

P. Givi
Associate Editor